Revealing Lithium Ion Transport Mechanisms and Solvation Structures in Carbonate Electrolytes

Authors: Junkun Pan[1], Aaron P. Charnay[1], Weizhong Zheng[2]*†, Michael D. Fayer[1]*‡

Affiliations:

[1] Department of Chemistry, Stanford University; Stanford, 94305, USA.

[2] State Key Laboratory of Chemical Engineering, School of Chemical Engineering, East China University of Science and Technology; Shanghai, 200237, China

*Corresponding author. Emails: wzzheng@ecust.edu.cn (WZ), fayer@stanford.edu (MDF)

† Requests for materials regarding MD simulation should be sent to this author.

‡ Requests for materials regarding experiments should be sent to this author.

Abstract

Optimizing lithium-ion battery (LIB) electrolytes is essential for high-current applications such as electric vehicles, yet experimental techniques to characterize the complex structural dynamics within these electrolytes are limited. These dynamics are responsible for Li^+ transport. In this study, we used ultrafast infrared spectroscopy to measure chemical exchange, spectral diffusion, and solvation structures across a wide range of lithium concentrations in propylene carbonate-based LiTFSI (lithium bis(trifluoromethanesulfonimide) electrolytes, with the CN stretch of phenyl selenocyanate as the long-lived vibrational probe. Phenyl selenocyanate is shown to be an excellent dynamical surrogate for propylene carbonate in Li^+ solvation clusters. A strong correlation between exchange times and ionic conductivity was observed. This correlation and other observations suggest structural diffusion as the primary transport mechanism rather than vehicular diffusion. Additionally, spectral diffusion observables measured by the probe were directly linked to the de-solvation dynamics of the Li^+ clusters, as supported by density functional theory and molecular dynamics simulations. These findings provide detailed

molecular-level insights into LIB electrolytes' transport dynamics and solvation structures, offering rational design pathways to advanced electrolytes for next-generation LIBs.

1. Introduction

The commercialization of lithium-ion batteries (LIBs) is one of the most influential technological advances in the last few decades.[1] As LIBs became the primary energy storage technology for many emerging applications, such as electric vehicles (EVs), the demands for battery performance have quickly outpaced the incremental refinements in lithium-ion technology.[2] LIB electrolyte compositions have barely changed since their initial employment.[3] In a battery cell, the electrolyte is responsible for transporting the ionic species between the cathode and anode. For the high-rate charging and discharging required for EV operation and other applications, slow lithium-ion transport in the electrolyte phase can lead to overpotentials in the graphite anode, causing reduced battery lifespan and internal short circuits caused by lithium plating.[4] Therefore, optimizing the ion transport properties of electrolytes is necessary for achieving DOE's goal of extreme fast charging (XFC): reaching 80% state of charge within 15 minutes.[5, 6]

One of the significant roadblocks to accomplishing this goal is the lack of characterization techniques for transport properties.[4, 7, 8] Currently, the mainstream experimental methods for studying the transport properties are electrical impedance spectroscopy (EIS) for ionic conductivity[9, 10] and pulsed-field gradient nuclear magnetic resonance (PFG-NMR) for self-diffusion coefficients.[11, 12] Although both methods have been extensively used for characterizing the bulk transport properties to quantify the electrolyte performance, recent work by Mistry and co-workers questions the appropriateness of using self-diffusivity measured by PFG-NMR to investigate ion transport in polarized electrolytes since the self-diffusivity-based Nernst Einstein relationship cannot accurately predict the measured conductivity in many electrolytes.[13] Therefore, developing and applying additional experimental methods to measure and understand

fast molecular-level dynamics and solvation structures required for the rational design of next-generation LIB electrolytes are valuable.

Ultrafast infrared (IR) spectroscopic methods have temporal resolution from femtoseconds to over a nanosecond depending on the vibrational probe lifetime, enabling the study of transport and related solvation dynamics in liquids.[14-17] Early efforts have attempted to use the native vibrational probes (C=O stretching mode) in carbonate electrolytes to measure the chemical exchange rate (interchange of Li^+ solvation partners); the observed chemical exchange time of several picoseconds was attributed to the solvent exchange in the Li^+ solvation shell.[18-20] However, it is now well-established that these extremely fast (<10 ps) observations originated from vibrational excitation transfer between neighboring carbonyls due to the high carbonyl concentration present in the solution.[21, 22] It is estimated that the lithium association and dissociation times are on the scale of hundreds of picoseconds to nanoseconds instead,[22, 23] which is impossible to observe with the short-lived (~2 ps) C=O vibrations.[20]

Consequently, the current knowledge regarding the fast dynamics and transport mechanisms in LIB electrolytes relies almost exclusively on molecular dynamics (MD) simulations.[24-27] However, MD studies give conflicting results regarding the fast dynamics in carbonate electrolyte systems. For example, Borodin and Smith reported the residence time of ethylene carbonate (EC) complexed with Li^+ is ~100 ps in 1 M LiTFSI/EC electrolyte.[28] In contrast, Self et al. reported the residence time between Li^+ and propylene carbonate (PC) in 1 M PC/$LiPF_6$ electrolyte to be on the order of nanoseconds, even though both simulations reproduce the bulk conductivities.[29] There is a lack of molecular-level experiments that can measure the relevant dynamics in the picosecond to nanosecond regime to bridge the gap between the bulk characterizations and the theoretical results.

In this study, ultrafast IR measurements were employed in combination with density functional theory (DFT) calculations and MD simulations to elucidate the transport mechanisms, solvation shell structures, and dynamics in PC electrolytes with LiTFSI salt over a significant concentration range (1.3 – 2.5 M, 1 ion pair per 7 PCs to 1 ion pair per 3 PCs). For IR measurements, a low-concentration of the vibrational probe phenyl selenocyanate (PSC) is added to the electrolytes, enabling an observation window from sub-picosecond to a nanosecond (CN stretching mode vibrational lifetime >300 ps (25)). In the electrolytes, PSC molecules can either be solvated by PCs or bind to Li^+ as part of its first solvation shell.[30] Binding to the lithium-ion causes the CN vibration to shift to a higher frequency and produce a spectral peak well-separated from that of PSCs solvated by PCs. This feature lets us distinguish the PSC molecules' environment based on the observed vibrational frequency and obtain dynamical information from the free (F) and Li-bound populations (L) separately.

We utilized two-dimensional infrared (2D IR) spectroscopy to measure the chemical exchange times between these two species and spectral diffusion (structural dynamics) as a function of LiTFSI concentrations. Unlike prior studies, the observed chemical exchange arises from lithium solvation shells' formation and dissociation dynamics, as confirmed by MD simulations, DFT calculations, and other experiments. The measured chemical exchange times slow as the LiTFSI concentration increases, and a linear correlation with the bulk ionic conductivities was observed. Additionally, the slowest component of the 2D IR spectral diffusion (structural randomization dynamics) of the Li^+-bound PSCs is shown to be caused by the dissociation events of the solvating molecules using a combination of DFT calculations and MD simulations. The simulated PC and PSC dissociation times are almost the same as the PSC dissociation times extracted from the chemical exchange experiments, vetting the simulations

and confirming the interpretation of the chemical exchange experiments. Using the dissociation times measured by 2D IR and Li^+ self-diffusion constants,[31] the characteristic Li^+ diffusion length is determined to be significantly smaller than the solvation shell radius, answering a fundamental question about Li^+ transport: the primary transport mechanism is structural transport rather than vehicular diffusion.

Finally, reorientation dynamics of the free PSCs and Li^+-complexed PSCs are measured using polarization-selective pump-probe (PSPP) spectroscopy. Free PSCs are shown to rotate much faster than those bound to Li^+ clusters, which reorient as a group in the electrolytes. The volumes of the solvation shells can be determined as a function of lithium salt concentration from the ratios of the complete reorientation times of the two species.[32] It was found that the average size of the first solvation shell increases with higher LiTFSI contents. Comparisons with the volumes calculated from DFT-optimized structures for various solvation shell compositions show that the dominant solvation shell is lithium coordinated to four PCs at low LiTFSI concentrations, which changes to three PCs and a $TFSI^-$ at high concentrations.

This study comprehensively characterizes the fast dynamic processes and sub-nanoscopic interactions underlying Li^+ bulk transport in PC/LiTFSI electrolytes. The ultrafast IR results were directly compared to the simulation, providing the much-needed experimental vetting of the MD simulations and enabling the development of better MD force fields. The discovered connection between spectral diffusion observables and de-solvation dynamics also enables the application of the same methodology to other LIB electrolytes, since structural randomization dynamics does not depend on the binding strength of the specific probe molecules.

2. Results and Discussions

2.1. FT-IR shows two PSC populations in equilibrium

The normalized linear absorption spectrums (FT-IR) of the CN stretching mode of PSC in PC with different LiTFSI concentrations are shown in Figure 1A. The lithium salt concentrations are given as the molar ratios of Li^+ to PC molecules. The five ratios studied in this work, from the highest to the lowest Li^+, are 1-3, 1-4, 1-5, 1-6, and 1-7, corresponding to a 1.3 M to 2.5 M concentration range. The probe concentration is kept at 250 mM for all samples, which was shown to be a low enough concentration that does not perturb the native dynamics (See supporting information (SI) for details). For pure PC (black dashed curve), the FT-IR spectrum only has one peak at ~2155 cm^{-1}, corresponding to the free PSC solvated in PC. However, with the addition of LiTFSI, a well-separated peak at ~2180 cm^{-1} appears, with its peak height directly correlated with the Li^+ concentration. These blue-shifted peaks are attributed to the PSC molecules bound to the lithium ions. As shown in Figure 1B, the full widths at half maxima (FWHMs) for the Li^+-bound peaks are significantly wider than the free peaks, indicating the probes' environments are more heterogeneous when part of the lithium solvation complexes. Additionally, higher LiTFSI concentration increases the width of the free PSC peak while the Li^+-bound peak becomes narrower. This data demonstrates that increased LiTFSI content changes the environment surrounding the free probes and modifies the average configuration of the Li^+ first solvation shell. The FT-IR spectra reflect the equilibrium configurations; below, 2D IR chemical exchange spectroscopy is employed to directly measure the interconversion between these two species.

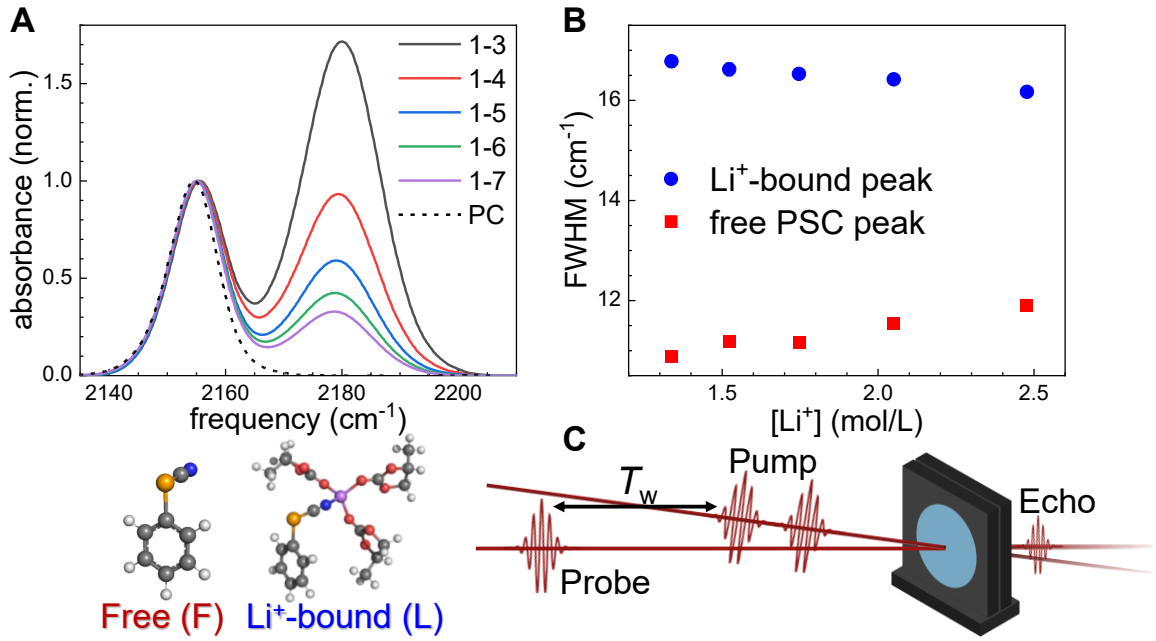

Fig. 1. The PSC probes exist in equilibrium between two distinct states in the electrolytes. (A) FT-IR spectra of PSC in pure PC (dashed line) and LiTFSI/PC electrolytes with different LiTFSI to PC ratios. The peak at 2155 cm^{-1} corresponds to the free probe molecules (F), and the peak at 2180 cm^{-1} arises from PSC molecules bound to lithium ions in solvation clusters (L). The spectra are normalized to the amplitude of the F peaks. The L band grows with increasing LiTFSI content. (B) Concentration-dependent full width at half maximum (FWHM) from double Gaussian fits to the FT-IR spectra of the two peaks. With increasing lithium salt concentration, the L peak's width narrows while the F peak becomes wider. (C) Schematic representation of 2D IR experimental pulse sequence.

2.2. Primary Transport Mechanism is Determined from Lithium Complexation Dynamics

2D IR spectroscopy measures the time evolution of the vibrational probes' frequencies, which reflects the changes in the surrounding molecular environments. In addition, when there are two peaks in equilibrium, 2D IR can directly measure the exchange rate between the two peaks.[15] 2D IR is a four-pulse sequence experiment (Figure 1C). The vibrational probes are excited by two pump pulses to label their initial frequencies. Then, the system is allowed to evolve for a waiting time (T_w), and a probe pulse stimulates the emission of the vibrational echo. The echo passes through a computer-controlled polarizer, a spectrograph, and an array detector, giving the final frequencies. Therefore, by systematically scanning T_w, the time evolution of the initial to final frequencies is measured. Additionally, by rotating the polarizer, 2D IR spectra can be measured in parallel ($S_{\parallel}$) or perpendicular ($S_{\perp}$) polarizations to the pump pulse. Then, the

isotropic 2D spectra can be obtained, $S_{iso} = (S_{||} + 2S_{\perp})/3$, eliminating the influence of orientational relaxation on the 2D spectra.[33]

Figures 2A and B display the normalized isotropic 2D IR spectra of PSC probes in the LiTFSI/PC electrolyte with a 1-5 ratio at two waiting times. The 2D spectra for other concentrations are given in Figure S1. The ω_{pump} axis gives the initial frequencies when the PSC molecules are excited by the pump pulses, and the ω_{probe} axis corresponds to the final frequencies obtained after the third pulse, which stimulates the emission of the vibrational echo pulse (the signal). At T_w = 1.5 ps (Figure 2A), the two diagonal peaks correspond to the two peaks in the FT-IR spectra: The low-frequency peak arises from the CN vibrations of the free PSC (denoted F), and the high-frequency peak is from the Li^+-bound PSC (denoted L). The negative off-diagonal peak (blue) arises from the 1-2 vibrational transition of the L species.[15] At T_w = 1.5 ps, the waiting time is too short for chemical exchange to occur. The final detected frequencies are the same as the initial frequencies, and the 0-1 transition peaks are only on the diagonal. At T_w = 400 ps (Figure 2B), some initially excited free PSCs become complexed with Li^+, producing an off-diagonal exchange peak (upper left corner). Similarly, some initially excited L population dissociates to free PSC, producing an exchange peak at the lower right corner. However, this peak is masked by the negative 1-2 peak and is not visible. Similar spectra were collected for T_ws between 1.5 ps and 450 ps to "watch" the growth and decay of the peaks. In addition to the growth of exchange peaks, changes in the peak shapes are caused by spectral diffusion, as discussed below.

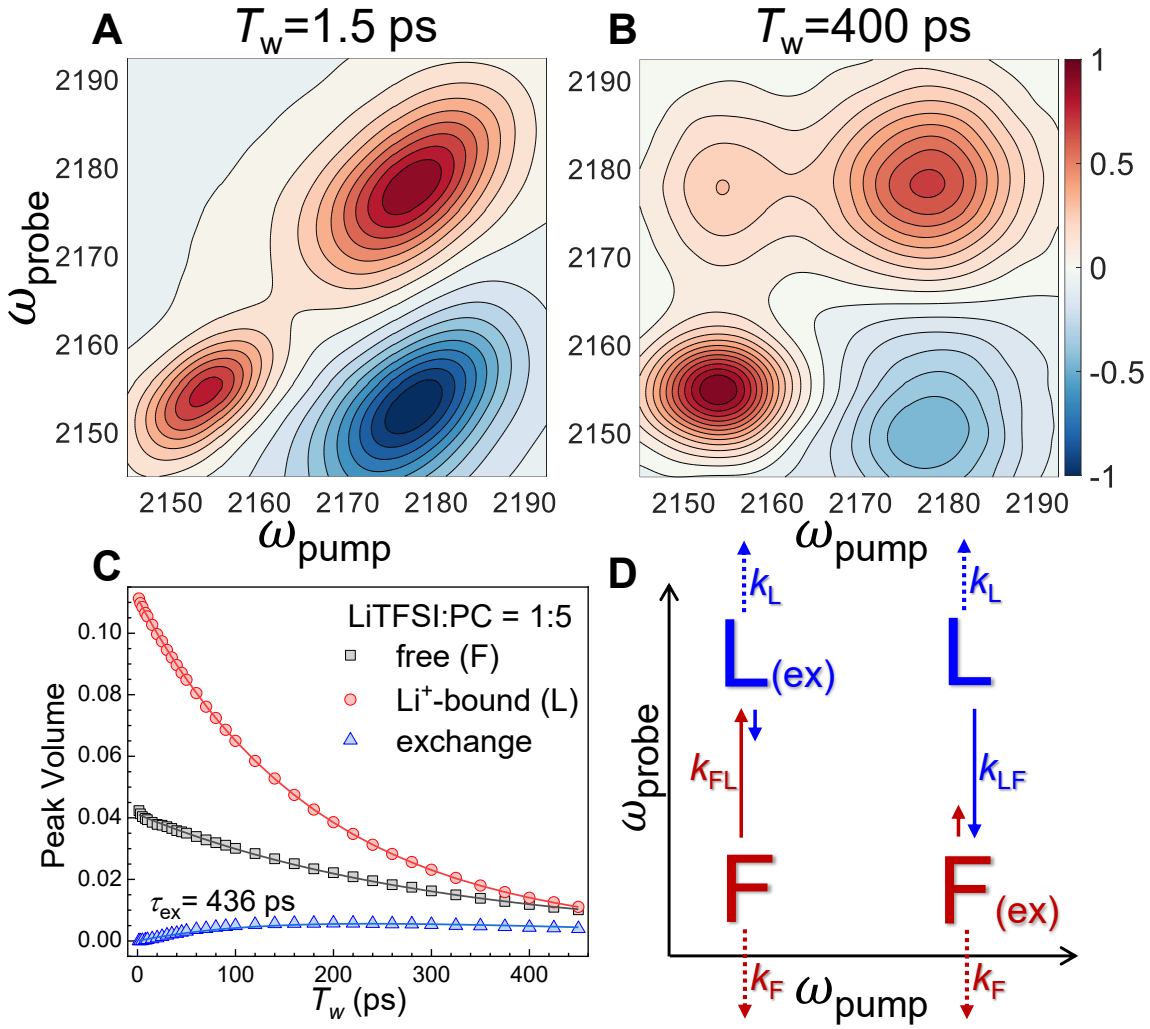

Fig. 2. Determination of primary transport mechanism from chemical exchange times. (A) Normalized (to the largest peak) 2D IR spectra of LiTFSI/PC electrolyte with 1-5 ratio at 1.5 ps delay time. Here, only three peaks are observed. (B) Normalized 2D IR spectra at 400 ps delay time. A fourth chemical exchange peak is present, which is attributed to free PSCs that become bound to a Li^+. (C) Time evolution of peak volumes for free PSCs, Li^+-bound PSCs, and the exchanged species in 1-5 LiTFSI/PC electrolytes. (D) Schematic representation of the exchange process in the 2D IR spectra and the corresponding rate constants.

The volume of each peak in the 2D spectrum is proportional to its population multiplied by the transition dipole strength to the fourth power. For the current system, the transition dipole ratio of peak F to peak L is 0.57 ± 0.01 (see SI for details). With this information, peak volumes were used to determine the evolution of the populations over time. The peak volumes were extracted by fitting the 2D spectra at each T_w with the sum of six 2D Gaussians, one for each

relevant peak in the 2D spectra, using the method described previously.[34] As shown in Figure S2, the fitted 2D spectra reproduce the experimental one exceptionally well.

Figure 2C shows the time evolution of the peak volumes corresponding to the F, L, and exchanged populations for the 1-5 sample. The time dependence of the peak volumes for other concentrations is given in Figure S3. Because the system is in equilibrium, the two exchange peaks have the same volumes at all times. Therefore, only one time-dependent volume is required to give the time dependence of the two exchange peaks. The peak volumes for F and L monotonically decrease with time, while the exchange peak volumes grow for ~150 ps and decay afterward. The contributions to the growth and decay of each peak volume are illustrated in Figure 2D. The labels' positions match their locations in the 2D IR spectrum in Figure 2B. Consider the peak labeled as F (bottom left); members of the subensemble that comprise F have a specific rate ($k_{FL)}$ bonding to a Li^+ and becoming part of the $L_{(ex)}$ population (top left). Additionally, the signal amplitude will decay from vibrational relaxation (k_F). The $L_{(ex)}$ peak first grows because of the chemical exchange from the F peak. Then, it will dissociate, returning to F with a different rate constant (k_{LF}) and undergo vibrational relaxation with constant k_L as an L species. The same processes happen in reverse for the peak labeled L (top right).

A quantitative two-species exchange kinetics model was developed previously to extract the rate constants from the time-dependent peak volumes in aqueous LiCl solutions [33]. Here, we adapted the model for application in carbonate electrolytes. The kinetic model was used with one set of parameters to simultaneously fit the three curves in Figure 2C. The details of the exchange kinetic equations are presented in the SI. The essential results here are the two exchange rate constant constants (k_{FL}, k_{LF}), which can be converted to association time ($\tau_a = 1/k_{FL}$) and dissociation/de-solvation time ($\tau_d = 1/k_{LF}$) for interpretation. In addition, the total exchange

time, which encompasses both processes, is $\tau_{ex} = 1/(k_{FL} + k_{LF})$. The time constants determined from the fit parameters for all concentrations are summarized in Table S1.

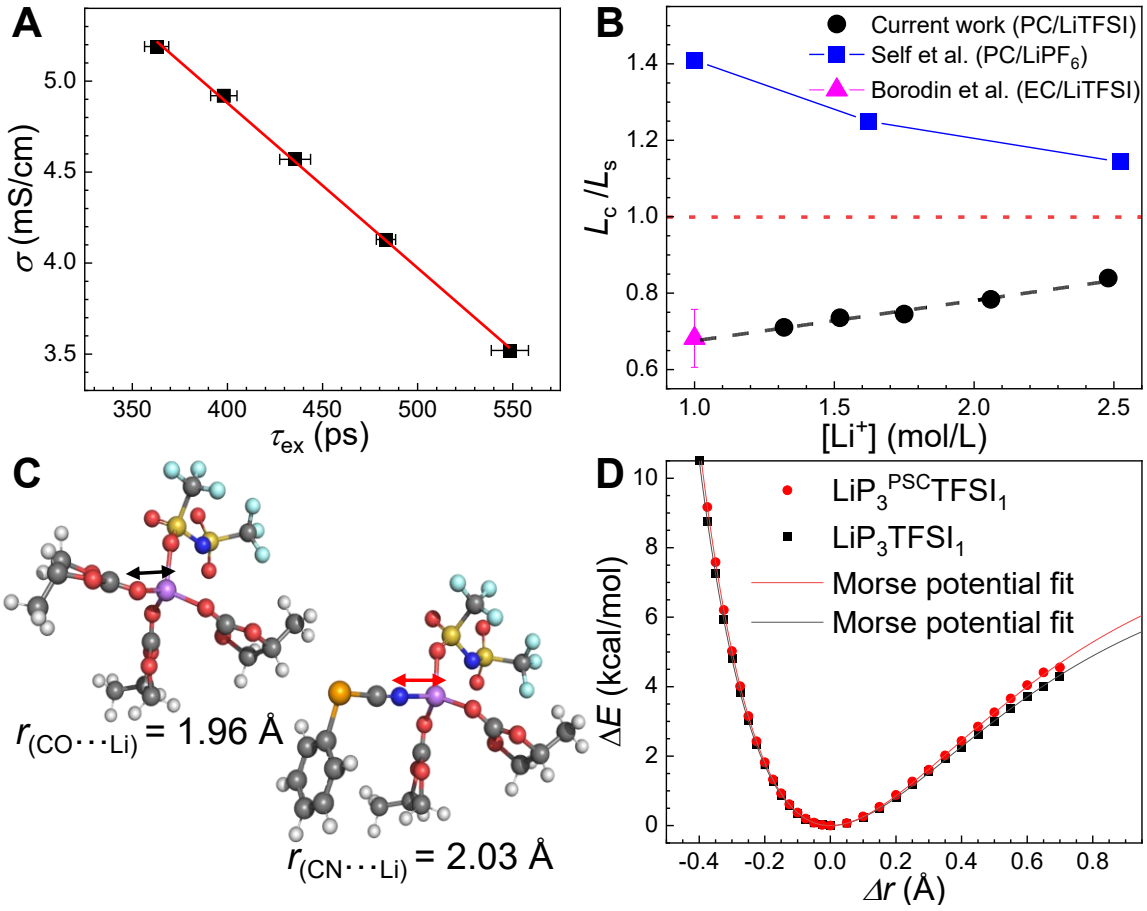

Fig. 3. Determination of transport mechanisms from de-solvation times. (A) Correlation between ionic conductivity from ref. 31 and total exchange times. The five data points are measured at different LiTFSI to PC ratios (decreasing concentration). (B) The ratio of the characteristic diffusion length (L_c) to the solvation shell radius. $L_c/L_s > 1$ means the primary transport mode is vehicular and $L_c/L_s < 1$ means structural diffusion dominates. The blue squares and the magenta triangle are L_c/L_s from MD simulations of similar systems from ref. 29 and ref. 28, respectively. (C) Geometry-optimized structures for Li^+ cluster consisting of 3 PCs plus 1 $TFSI^-$ and the same structure with a PC replaced by PSC. The arrows indicate the bonds used for calculating the potential energy surface scans (PES). (D) PES calculations for the bond length between Li^+ and CO/CN. The potentials can be described as pseudo-Morse potentials, and the fits reveal dissociation energies of 8.0 kcal/mol for LP_3TFSI_1, and 8.7 kcal/mol for $LP_3^{PSC}TFSI_1$.

Our results confirm that the chemical exchange between the free PSC and Li-bound PSC species in PC/LiTFSI electrolytes happens on the time scale of hundreds of picoseconds. The measured total exchange times slow from 363 ps to 552 ps, with the LiTFSI concentration increasing from 1.3 M to 2.5 M. Lithium transport can occur via structural diffusion or the

vehicular mechanism. In the structural diffusion mechanism, lithium diffusion is caused by the switching of solvation shell partners, inducing solvation shell rearrangement, which causes Li^+ to move to a new solvation site. In vehicular transport, the Li^+ diffuses with its solvation shell intact for relatively long distances. The relative importance of each mechanism is hard to disentangle because conductivity or diffusivity measurements can include contributions from both mechanisms.

The transport rate from the structural mechanism is directly related to how fast solvation clusters exchange components. Therefore, the time constants from our measurements provide a means to examine structural transport quantitatively. Figure 3A plots the exchange time (τ_{ex}) against the ionic conductivities from Seki et al.[31] The observed correlation is excellent. The correlation indicates a significant contribution to the total conductivity from the structural mechanism. The primary diffusion mode of Li^+ in carbonate electrolytes has been studied by comparing the characteristic Li^+ diffusion length (L_c) with its solvation shell to the solvation shell radius (L_s).[28, 29] L_c is the distance traveled by Li^+ before a solvation shell dissociation occurs. Therefore, if $L_c/L_s > 1$, Li^+ travels with its solvation cluster further than the radius of the solvation shell, and the principal diffusion mode is vehicular. For the reverse, $L_c/L_s < 1$, the Li^+ moves because of solvent shell reconfiguration (structural diffusion) before it travels a distance greater than the solvent shell radius with its solvation shell intact. L_c can be calculated from the residence time (τ_{res}^{PC}), that is, the time for a member of Li^+'s solvation shell to dissociate and its self-diffusion constant (D_{Li}) using the Einstein relation:[28]

$$L_c = \sqrt{6 D_{Li} \tau_{res}^{PC}} \,. \qquad (1)$$

This quantity has been used in MD studies.[29] With the ability to experimentally measure the dissociation time, we can apply this method for determining the nature of Li^+ transport in our

systems. One caveat is that the τ_d (τ_{res}^{PC}) measured with our method is for PSC in the Li^+ solvation shell rather than for PC; however, it will be shown below using a combination of DFT calculations, MD simulations, and 2D IR spectral diffusion experiments that the dissociation time from the lithium cluster is virtually identical for PSC and PC. For the following analysis, $\tau_d^{PSC} = \tau_{res}^{PC}$.

D_{Li} is from the PFG-NMR measurements reported by Seki et al.[31] Given these considerations, the calculated L_c increased from 4.7 Å to 5.7 Å with increased LiTFSI concentration. The solvation shell radius was determined from MD simulations to be 6.6 Å using the definition from Self et al.[29] (see SI). This value agrees with their L_s value in PC/$LiPF_6$ electrolytes. The L_c/L_s ratios at each concentration are shown as the black circles in Figure 3B. For all concentrations, the ratio is less than one, demonstrating that structural diffusion is the dominant mechanism, which is consistent with our observations showing the correlation between τ_{ex} and ionic conductivity (Figure 3A). L_c/L_s increases from 0.71 to 0.86 with higher salt contents, showing a more significant but still reasonably small vehicular component. The black dashed line through the data points (Figure 3B) is a linear fit. The magenta triangle in Figure 3B shows the L_c/L_s value for 1 M LiTFSI ethylene carbonate (EC) reported by Borodin et al.[28] from MD simulations. Although this concentration is beyond the range studied here, the linear fit extrapolated from our results is in excellent agreement with their simulation. In contrast, the L_c/L_s reported by Self et al. (Figure 3B blue squares)[29] from MD simulations of the $LiPF_6$/PC system are significantly larger than 1. Their simulation results indicated that the vehicular mechanism is dominant, which is inconsistent with the experimental results presented here although the anions in the two studies are different.

We have verified that the dissociation times of PSC and PC from lithium clusters are virtually the same as discussed here, with more details in the supporting information. We performed DFT calculations of the lithium-ion solvation shell clusters. Geometry optimizations were performed using implicit PC solvents with different cluster compositions at the PBE/6-31G+(d,p) level of theory[35]. One of the clusters with three PCs and one TFSI is shown in Figure 3C. After the initial optimization, one of the PCs in each cluster was replaced by a PSC and re-optimized, ensuring minimal variations from different initial geometries in the rest of the structure. Frequency calculations confirmed the absence of imaginary frequencies. It is worth noting that the DFT CN stretch vibrational frequency agrees with the experimental value within 1 cm^{-1}.

Comparing the two analogous structures in Figure 3C, the bond length between CO···Li is 1.96 Å, and the bond length between CN···Li is 2.03 Å, a difference of only 0.07 Å. Additionally, the differences in all bond angles between the pair of clusters are within 5°. This evidence suggests that PSC behaves similarly to PC in the lithium solvation clusters. A relaxed potential energy surface scan was performed for CO···Li and CN···Li bond lengths (Figure 3D) with the rest of the cluster re-optimized at each step. The two curves are nearly identical around the minimum of the potential well, with the PSC energy rising slightly more steeply for $\Delta r > 0.5$ Å, suggesting PSC dissociation will be somewhat slower than PC. The calculated energy can be described well by pseudo-Morse potentials. The fits reveal a Morse-like dissociation energy difference of 8%. Calculations of clusters with other compositions resulted in similar conclusions (Figure S4). The DFT calculations demonstrate that PSC and PC have similar binding potential to the Li^+ cluster around the minimum, with PC having slightly smaller binding energy. As

presented below, the similarity of the PSC and PC dissociation is substantiated by MD simulations, with further evidence provided by spectral diffusion data of Li^+-bound PSC.

2.3. The slowest Li-bound PSC Spectral Diffusion Component is Caused by Li^+ cluster PC Dissociation Events.

The IR absorption bands of PSC shown in Figure 1A are inhomogeneously broadened. Due to different intermolecular interactions, distinct PSC environments give rise to distinct CN absorption frequencies. These distinct frequencies comprise the inhomogeneous absorption band. Structural dynamics in the vicinity of the probe cause the intermolecular interactions to change with time, which, in turn, cause the frequencies of the PSCs to evolve. The time evolution of the frequencies is called spectral diffusion. The time dependence of spectral diffusion is directly related to the time-dependent structure.

2D IR spectroscopy can measure spectral diffusion dynamics by analyzing the T_w-dependent 2D band shapes. The 2D spectra give the correlations between the initial and final frequencies. Because free and Li^+-bound PSC species exist in equilibrium with a relatively slow interconversion rate, the spectral diffusion dynamics can be measured separately for the free PSCs and the Li^+-bound PSCs, yielding distinct information. At an early T_w (1.5 ps), when little time has elapsed for spectral diffusion (structural changes) to occur, the initial and final frequencies are highly correlated, and the band shape is elongated along the diagonal (Figure 2A). The frequency correlations are lost as T_w increases because environments around the probe molecules change. The band shape is almost circular for a late T_w (400 ps, Figure 2B). The changes in 2D lineshapes can be quantified using the central line slope (CLS) method, which gives the normalized frequency-frequency correlation function (FFCF), the connection between the 2D IR observable and the molecular-level dynamics.[36, 37] The CLS method has been

extensively applied to characterize the fast structural dynamics in a wide variety of solids, proteins, and liquids, including electrolytes.[38-40] The presence of overlapping exchange peaks complicates the determination of the CLS decays. A proven method is applied to overcome this complication.[39] (see Figure S5 and section S2.4)

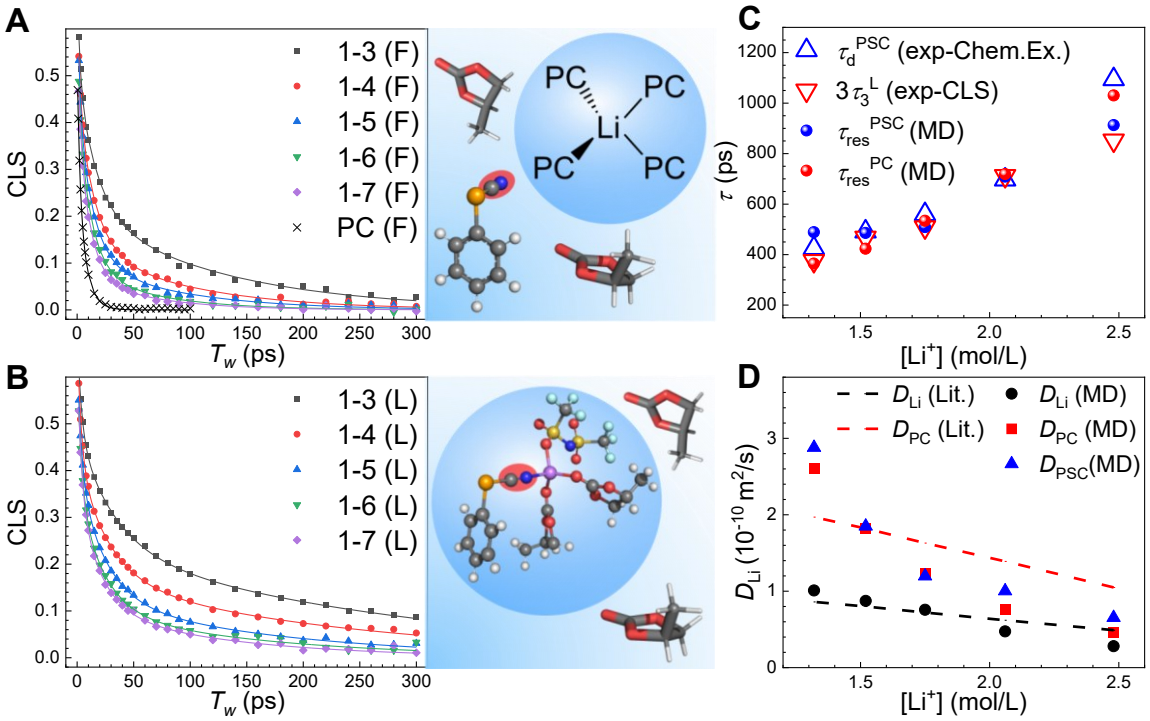

Fig. 4. Spectral diffusion dynamics and MD simulation. (A) isotropic CLS decays for the free (F) PSC in LiTFSI/PC electrolytes and pure PC (crosses). A schematic depicting the environments surrounding the free probes is shown to the right. Pure PC's CLS is a biexponential decay, while the CLS's of the electrolytes are triexponential decays (solid lines are fits). (B) isotropic CLS decays for the Li-bound PSC (L) in LiTFSI/PC electrolytes. The lines are triexponential decay fits to the data (points). To the right is a schematic showing the PSC's CN frequency is shielded from the dynamics outside the cluster. (C) Comparisons among PSC dissociation times, spectral diffusion time constants, and MD residence times. Blue open triangles are the PSC dissociation times from chemical exchange experiments. Red open upside-down triangles are the slowest CLS decay time constants of Li-bound PSCs multiplied by 3. Blue and red spheres are the PSC-Li and PC-Li residence times from the MD simulations, respectively. The simulated PSC-Li residence time agrees with the experimental PSC dissociation times. The simulated PC dissociation matches $3\tau_3^L$ from the CLS. (D) Self-diffusion coefficients for Li^+, PC, and PSC from MD simulations. The dashed lines are extrapolations from two experimental data points from ref. 31.

Multiple mechanisms contribute to the decorrelation of the frequencies (CLS decay), namely, exchange-induced spectral diffusion (EISD), reorientation-induced spectral diffusion (RISD), and structural spectral diffusion (SSD).[33, 41] However, the contributions from EISD and

RISD are small and can be ignored safely (see SI section S2.3). Consequently, the CLS decays characterize structural changes in the proximities of the probes.

Figure 4A displays the isotropic CLS decays of free PSC species in pure PC and in LiTFSI/PC electrolytes and a schematic representation of the environment surrounding free PSCs. The fastest CLS decay is from the free PSC in pure PC. The decay is biexponential with the first time constant, $\tau_1^F = 2.2 \pm 0.3$ ps, and the second time constant, $\tau_2^F = 7.2 \pm 0.5$ ps. In pure PC, the decorrelation of CN vibrational frequency can only be affected by the dynamics of PC molecules. Given the fast timescale, τ_1^F may be caused by translational fluctuations of the solvent molecules. τ_2^F is on the same time scale as the orientational wobbling motions of small molecules similar to those measured here by the PSPP experiments discussed below (Table S1) and is attributed to PCs' configuration fluctuations. With the addition of LiTFSI salts, the CLS becomes tri-exponential with a third decay component characterized by a much slower time constant, τ_3^F (59-125 ps). At high Li^+ concentrations studied here, free PSCs will be surrounded by PCs, TFSIs, and Li^+ solvation clusters, as shown by the scheme in Figure 4A. The vibrational frequencies of the probes will be sensitive to the motions of all components of their environments; therefore, τ_3^F is attributed to the ion cluster dynamics. As expected, the dynamics of free PC (τ_2^F) and ion clusters (τ_3^F) slow down with increasing LiTFSI content, likely due to increased viscosity.

The CNs of Li^+-bound PSCs are in the interiors of the first solvation shells of Li^+s. The CN vibrations are sequestered from the free solvent environment and will principally be influenced by the dynamics of the complexes. Consequently, the Li-bound PSCs' CLS decay measures structural changes within the solvation cluster. Figure 4B displays the isotropic CLS

decays for the Li-bound PSCs and the scheme of the cluster environment. The CLS decays are tri-exponential and are slower than the free probes' CLS of the same concentrations (See Table S2 for complete sets of spectral diffusion time constants). Similar to the assignments of free PSC's CLS time constants, the first two exponential decay time constants (τ_1^L and τ_2^L) are attributed to the $CN^{\cdots}Li^+$ bond fluctuations and the configurational motions of the solvation shell partners (Li-bound PC/$TFSI^-$), respectively.

Given that τ_3^L is significantly slower than τ_3^F, and is largely shielded from the surrounding solvent dynamics, τ_3^L arises from a distinct dynamical process within the Li-complex. τ_3^L is in the range of ~200 ps; only one dynamic process within the cluster can cause frequency decorrelation on this time scale. We propose that τ_3^L characterizes the de-solvation process, specifically, the dissociation of Li^+ solvation components. Dissociation of a PC or $TFSI^-$ from a Li^+ complex will occur with significant structural changes. These changes will induce the complete loss of frequency correlation, which gives rise to the slowest spectral diffusion time constant. For the dissociation events to be observed, a PSC has to remain in the cluster, which leaves three other possible dissociation pathways for a total lithium coordination number of four [42, 43]. Since any of the three cluster components leaving would cause the frequency decorrelation, τ_3^L measures the total rate of all three pathways. Therefore, the average dissociation time of a single component will take three times as long ($3\tau_3^L$). A similar correction has been applied to a 2D IR study of concentrated HCl solutions to extract proton hopping dynamics.[44] The PSPP experiment described below will show the dominant cluster composition is four PCs at low concentrations and three PCs plus a $TFSI^-$ at high concentrations. Given the cluster compositions, $3\tau_3^L$ is equal to the PC dissociation time at low concentrations. At higher

concentrations, it is the average dissociation time of two PCs and one $TFSI^-$. In the section above, we discussed the dissociation times of PSCs measured from the chemical exchange and used DFT to suggest that the dissociation times of PCs and PSCs are virtually the same. In Figure 4C, the blue open triangles are the experimental PSC dissociation time (τ_d^{PSC}) extracted from the chemical exchange experiments, and the red upside-down open triangles are $3\tau_3^L$ from the Li^+-bound PSC's CLS decays, which measure the average time for dissociation of one of the components of the solvation shell that is not PSC. τ_d^{PSC} and $3\tau_3^L$ are distinct observables. Nonetheless, the data for the two observables are exceedingly close, providing strong evidence for our interpretation of the slowest CLS component as a measure of solvation shell component dissociation. The results that τ_d^{PSC} and $3\tau_3^L$ are almost the same demonstrate that the times for PSC dissociation and PC dissociation are essentially identical, agreeing with the DFT results discussed above.

MD simulations were conducted to provide information on aspects of the experimental studies that cannot be directly measured and to vet both experimental conclusions and the simulations. All-atom MD simulations were performed with a modified OPLA-AA force field for LiTFSI/PC/PSC systems of the same molar ratios as the experiments. The force field parameters for the PSC probes were modified to reproduce the experimental orientational anisotropy data, $r(t)$, presented below (Figure S6A), and the parameters for PC were slightly tuned to accurately reproduce the Li^+ self-diffusion coefficients (D_{Li}) measured by Seki et al.[31] The complete simulation details are provided in the SI. The black and red dashed lines in Figure 4D connect the two available experimental points from the literature,[31] which fall outside the concentration range of the plot. The black dashed line is the experimental D_{Li}, and the black squares are the MD simulated D_{Li} at each concentration; they demonstrate excellent agreement.

Similarly, the experimental self-diffusion coefficient of PC (D_{PC})[31] is represented by the red dashed line, and the simulated D_{PC} and PSC self-diffusion coefficients (D_{PSC}) are shown as red squares and blue triangles, respectively. The simulated values of D_{PC} and D_{PSC} match closely, reflecting their nearly identical dynamical behavior, consistent with their similarity in sizes and shapes. The agreement between the experimental D_{PC} and its simulation is not as good, but it is still reasonable.

The MD results and the dissociation times measured by 2D IR are compared by analyzing the residence times for PC and PSC complexed with Li^+ following similar procedures to those reported previously.[28, 29] In Figure 4C, the simulated Li-PSC residence times are plotted as blue spheres, and the computed Li-PC residence times are plotted as red spheres. The residence times derived from MD simulations closely match the PSC dissociation times measured by chemical exchange and the PC dissociation times obtained from the CLS decays. This substantial agreement indicates that the dissociation times obtained from 2D IR chemical exchange are very close to the residence times from MD simulations. It also supports our previous assignment of τ_3^L to the dissociation events of components of the Li^+ solvation cluster. These results demonstrate that PSC is an accurate dynamical surrogate for PC confirming our interpretations of the data.

2.4. Rotational Dynamics and the Solvation Shell Compositions

The rotational dynamics of PSC in PC/LiTFSI electrolytes were examined using PSPP spectroscopy, which was then analyzed to determine the solvation shell compositions. Like spectral diffusion dynamics, the rotational dynamics of free and Li-bound PSCs can be measured separately for the two populations. The observable for the PSPP experiment is the anisotropy decay, $r(t)$, which quantifies the orientational relaxation of the CN transition dipole of the

vibrational probe as a function of t (see SI for details). The $r(t)$ of PSC in PC/LiTFSI electrolytes and pure PC are presented in Figure 5A. The $r(t)$ decays slow down significantly with increasing LiTFSI concentration. Additionally, the anisotropies are separated into two distinct groups, with the Li^+ solvation clusters' (L) reorientation much slower than the free PSC (F). The decays are multi-exponentials. On short time scales, from 10 ps to 30 ps, the probe samples a restricted range of angles, the cone. On a longer time scale, the probe undergoes complete orientation randomization. Note that the Li^+ solvation cluster undergoes orientational randomization as a unit. The complete reorientation times (τ_m) can be extracted from the anisotropy using the well-established wobbling-in-a-cone (WIAC) model.[45-47] Here, only the complete orientation randomization time constant, τ_m, is necessary for the analysis. The details of the analysis and the time constants from the WIAC fits are given in the SI (Table S1).

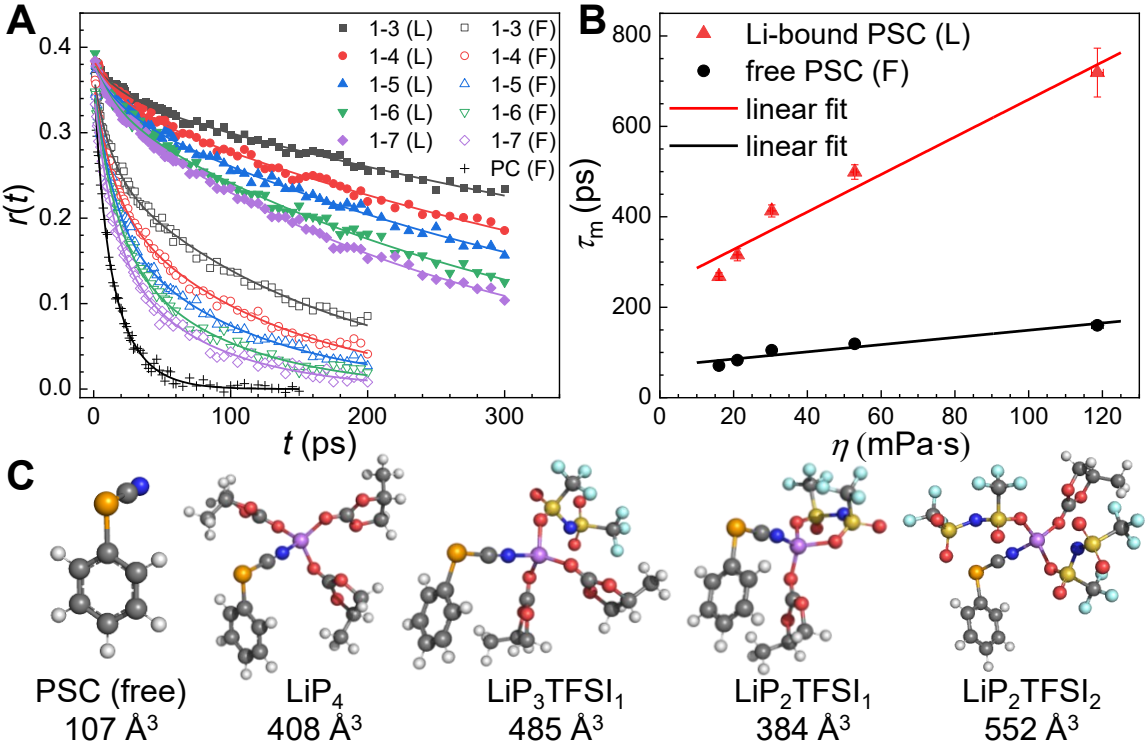

Fig. 5. Rotational dynamics and optimized solvation shell structures. (A) Anisotropy decay, $r(t)$, of PSCs in Li^+ solvation clusters (L) and free PSCs (F) in LiTFSI/PC electrolytes with molar ratios of 1-3 to 1-7. The black plus signs show $r(t)$ for PSC in pure PC. (B) Total reorientation time (τ_m) vs viscosity. τ_m increases linearly with viscosity for both F and L species, obeying fractional SED law. (C) DFT-optimized structures for free PSC and lithium solvation clusters with their respective solvent-excluded volumes.

In the Stokes-Einstein-Debye (SED) equation, τ_m is proportional to the viscosity (η) and the volume (V) of the rotator:[48]

$$\tau_m = \frac{\eta V}{k_B T} \quad (2)$$

Equation 2 is the general SED model for spherical rotators with stick boundary conditions. Modifications have been made to the general SED equation using correction factors,[49, 50] extending the application to systems that exhibit fractional SED behaviors. It has been shown that dilute PC electrolytes obey the general SED equation, and many electrolyte systems operate under the fractional SED regime.[51]

The τ_m vs. solution viscosity plots for both F and L populations in the LiTFSI/PC electrolytes are shown in Figure 5B. τ_m vs. viscosity for both PSC populations display a linear relationship; however, the linear fit has a non-zero offset, indicating the reorientation of PSCs in LiTFSI/PC solutions shows fractional SED behavior. Since the F and L populations experience the same bulk viscosity for a particular electrolyte solution, the difference in orientational relaxation rate originates from the difference in the volume of the rotating moieties, and the τ_m ratio gives the hydrodynamic volume ratio:

$$\frac{\tau_m^L}{\tau_m^F} = \frac{V_L}{V_F}. \quad (3)$$

Similar approaches have been applied to other electrolyte systems to investigate the cation coordination numbers.[32, 52] The ratios of the complete reorientation times for the five electrolyte systems in the order of increasing Li^+ concentration are 3.8 ± 0.2, 3.8 ± 0.2, 3.9 ± 0.2, 4.2 ± 0.2, and 4.5 ± 0.4, respectively. The volume of the free PSC was determined to be 107 $Å^3$ by applying Connolly's solvent-excluded volume method[53] on the geometry-optimized structures.

Therefore, the average volume of the solvation shell cluster increases from 400 $Å^3$ to 480 $Å^3$ as LiTFSI concentration increases.

We conducted DFT calculations on the possible structures to investigate the corresponding solvation sheath compositions that give rise to these average volumes. Because the anisotropy measurements were performed on the PSC's CN mode, the observed solvation sheath will always have one PSC, replacing a PC molecule in the normal solvation shell. As discussed previously, PSC does not significantly alter the solvation shell structure (Figure 3C) and is similar to PC in size. Additionally, it is generally accepted that Li^+ favors a coordination number of four in PC electrolytes,[42, 43] so we investigated clusters with the following compositions: LiP_4, LiP_3TFSI_1, LiP_2TFSI_1, LiP_2TFSI_2, LiP_1TFSI_2, where LiP_xTFSI_y denotes cluster with *x* PC/PSC, and *y* $TFSI^-$. The geometry-optimized structures and their respective volumes are presented in Figure 5C. At the lower concentrations, the average volume determined from our anisotropy measurements matches very well with the volume of the LiP_4 cluster (408 $Å^3$), which shows that coordination of four PCs is the dominant solvation shell cluster composition. With increasing LiTFSI concentration, the observed cluster volume increases, which can be explained by the increasing concentration of Li^+-$TFSI^-$ contact ion pairs in the electrolytes. At the highest concentration studied (1-3), the average volume is 480 $Å^3$, essentially identical to the LiP_3TFSI_1's volume of 485 $Å^3$. The measurements here are the average volumes of all structures present at a particular concentration. Structures such as LiP_2TFSI_1, LiP_2TFSI_2, and LiP_1TFSI_2 have volumes that are not in accord with the orientation relaxation measurements and therefore do not occur to a significant extent.

3. Concluding Remarks

The ultrafast IR spectroscopy and simulations described in this study provide a comprehensive analysis of the transport mechanisms, solvation dynamics, and structures of propylene carbonate electrolytes with high concentrations of LiTFSI salt. By employing phenyl selenocyanate as a vibrational probe, we successfully measured the chemical exchange rates and spectral diffusion dynamics over a significant range of concentrations. Furthermore, the efficacy of phenyl selenocyanate as a vibrational probe for measuring dynamics in carbonate electrolytes was validated by DFT calculations and MD simulations. The results show that the solvent exchange times are correlated with concentration-dependent ionic conductivities, and the ratio of the characteristic diffusion length (L_c) to the solvation shell radius (L_s) is less than one ($L_c/L_s < 1$). These findings highlight structural diffusion as the primary lithium transport mechanism. The ultrafast IR techniques employed in this study can be applied to other electrolyte systems, such as ether-based electrolytes[54] and gel-polymer electrolytes,[55] providing a versatile approach for investigating transport properties and solvation dynamics across a wide variety of materials. The dynamical and structural information obtained enhances our understanding of the nanoscopic interactions and dynamics that underpin the bulk transport properties in lithium-ion battery electrolytes. The results presented here and future studies of other liquid electrolytes and gel polymer electrolytes can accelerate the development of advanced LIB electrolytes.

Associated Content

Supporting Information

The Supporting Information is available free of charge at

https://pubs.acs.org/xxxxxxxxxxxxxxxxxx

Experimental Methods, Determination of transition dipole ratio, Two species exchange kinetics, The main contribution to CLS decay is SSD, 2D Gaussian fits and peak subtractions for CLS extraction, and Influence of probe concentrations.

Author Information

Corresponding Authors

Weizhong Zheng − State Key Laboratory of Chemical Engineering, East China University of Science and Technology, Shanghai 200237, China

orcid.org/0000-0002-3866-4932

Phone: (021) 64253175

Email: wzzheng@ecust.edu.cn

Michael D. Fayer − Department of Chemistry, Stanford University, Stanford, California 94305, United States

orcid.org/0000-0002-0021-1815

Phone: (650) 723-4446

Email: fayer@stanford.edu

Authors

Junkun Pan − Department of Chemistry, Stanford University, Stanford, California 94305, United States

orcid.org/0000-0001-6128-1844

Aaron P. Charnay − Department of Chemistry, Stanford University, Stanford, California 94305, United States

orcid.org/0000-0003-1797-9465

Complete contact information is available at:
https://pubs.acs.org/xxxxxxxxx

Notes

The authors declare no competing financial interest.

Acknowledgments

This work was supported by the National Science Foundation, Division of Chemistry, award number 2319637. Part of this work was performed at the Stanford Nano Shared Facilities (SNSF), supported by the National Science Foundation under award ECCS-2026822.

References

(1) Armand, M.; Axmann, P.; Bresser, D.; Copley, M.; Edström, K.; Ekberg, C.; Guyomard, D.; Lestriez, B.; Novák, P.; Petranikova, M.; et al. Lithium-ion batteries - Current state of the art and anticipated developments. *J. Power Sources* **2020**, *479*, 228708.

(2) Deng, J.; Bae, C.; Denlinger, A.; Miller, T. Electric Vehicles Batteries: Requirements and Challenges. *Joule* **2020**, *4*, 511-515.

(3) Xu, K. Electrolytes and interphases in Li-ion batteries and beyond. *Chem. Rev.* **2014**, *114*, 11503-11618.

(4) Logan, E. R.; Dahn, J. R. Electrolyte Design for Fast-Charging Li-Ion Batteries. *Trends in Chemistry* **2020**, *2*, 354-366.

(5) Wang, C. Y.; Liu, T.; Yang, X. G.; Ge, S.; Stanley, N. V.; Rountree, E. S.; Leng, Y.; McCarthy, B. D. Fast charging of energy-dense lithium-ion batteries. *Nature* **2022**, *611*, 485-490.

(6) Weiss, M.; Ruess, R.; Kasnatscheew, J.; Levartovsky, Y.; Levy, N. R.; Minnmann, P.; Stolz, L.; Waldmann, T.; Wohlfahrt-Mehrens, M.; Aurbach, D.; et al. Fast Charging of Lithium-Ion Batteries: A Review of Materials Aspects. *Adv. Energy Mater.* **2021**, *11*, 2101126.

(7) Meng, Y. S.; Srinivasan, V.; Xu, K. Designing better electrolytes. *Science* **2022**, *378*, eabq3750.

(8) Fawdon, J.; Ihli, J.; Mantia, F.; Pasta, M. Characterising lithium-ion electrolytes via operando Raman microspectroscopy. *Nat. Commun.* **2021**, *12*, 4053.

(9) Zeng, Y.; Ouyang, B.; Liu, J.; Byeon, Y. W.; Cai, Z.; Miara, L. J.; Wang, Y.; Ceder, G. High-entropy mechanism to boost ionic conductivity. *Science* **2022**, *378*, 1320-1324.

(10) Wang, S.; Zhang, J.; Gharbi, O.; Vivier, V.; Gao, M.; Orazem, M. E. Electrochemical impedance spectroscopy. *Nature Reviews Methods Primers* **2021**, *1*, 41.

(11) Han, K. S.; Bazak, J. D.; Chen, Y.; Graham, T. R.; Washton, N. M.; Hu, J. Z.; Murugesan, V.; Mueller, K. T. Pulsed Field Gradient Nuclear Magnetic Resonance and Diffusion Analysis in Battery Research. *Chem. Mater.* **2021**, *33*, 8562-8590.

(12) Richardson, P. M.; Voice, A. M.; Ward, I. M. Two distinct lithium diffusive species for polymer gel electrolytes containing LiBF4, propylene carbonate (PC) and PVDF. *Int. J. Hydrogen Energy* **2014**, *39*, 2904-2908.

(13) Mistry, A.; Yu, Z.; Peters, B. L.; Fang, C.; Wang, R.; Curtiss, L. A.; Balsara, N. P.; Cheng, L.; Srinivasan, V. Toward Bottom-Up Understanding of Transport in Concentrated Battery Electrolytes. *ACS Cent. Sci.* **2022**, *8*, 880-890.

(14) Park, S.; Kwak, K.; Fayer, M. D. Ultrafast 2D-IR vibrational echo spectroscopy: a probe of molecular dynamics. *Laser Phys. Lett.* **2007**, *4*, 704-718.

(15) Zheng, J.; Kwak, K.; Asbury, J.; Chen, X.; Piletic, I. R.; Fayer, M. D. Ultrafast dynamics of solute-solvent complexation observed at thermal equilibrium in real time. *Science* **2005**, *309*, 1338-1343.

(16) Lee, K. K.; Park, K. H.; Kwon, D.; Choi, J. H.; Son, H.; Park, S.; Cho, M. Ion-pairing dynamics of Li+ and SCN- in dimethylformamide solution: chemical exchange two-dimensional infrared spectroscopy. *J. Chem. Phys.* **2011**, *134*, 064506.

(17) Park, K. H.; Choi, S. R.; Choi, J. H.; Park, S.; Cho, M. Real-time probing of ion pairing dynamics with 2DIR spectroscopy. *Chemphyschem* **2010**, *11*, 3632-3637.

(18) Lim, J.; Lee, K. K.; Liang, C.; Park, K. H.; Kim, M.; Kwak, K.; Cho, M. Two-Dimensional Infrared Spectroscopy and Molecular Dynamics Simulation Studies of Nonaqueous Lithium Ion Battery Electrolytes. *J. Phys. Chem. B* **2019**, *123*, 6651-6663.

(19) Liang, C.; Kwak, K.; Cho, M. Revealing the Solvation Structure and Dynamics of Carbonate Electrolytes in Lithium-Ion Batteries by Two-Dimensional Infrared Spectrum Modeling. *J. Phys. Chem. Lett.* **2017**, *8*, 5779-5784.

(20) Lee, K. K.; Park, K.; Lee, H.; Noh, Y.; Kossowska, D.; Kwak, K.; Cho, M. Ultrafast fluxional exchange dynamics in electrolyte solvation sheath of lithium ion battery. *Nat. Commun.* **2017**, *8*, 14658.

(21) Lim, C.; Jeon, J.; Park, K.; Liang, C.; Chae, Y.; Kwak, K.; Cho, M. Revisiting Ultrafast Dynamics in Carbonate-Based Electrolytes for Li-Ion Batteries: Clarifying 2D-IR Cross-Peak Interpretation. *J. Phys. Chem. B* **2023**, *127*, 9566-9574.

(22) Dereka, B.; Lewis, N. H. C.; Zhang, Y.; Hahn, N. T.; Keim, J. H.; Snyder, S. A.; Maginn, E. J.; Tokmakoff, A. Exchange-Mediated Transport in Battery Electrolytes: Ultrafast or Ultraslow? *J. Am. Chem. Soc.* **2022**, *144*, 8591-8604.

(23) Shah, N. J.; Fang, C.; Osti, N. C.; Mamontov, E.; Yu, X.; Lee, J.; Watanabe, H.; Wang, R.; Balsara, N. P. Nanosecond solvation dynamics in a polymer electrolyte for lithium batteries. *Nat. Mater.* **2024**, *23*, 664-669.

(24) Kumar, N.; Seminario, J. M. Lithium-Ion Model Behavior in an Ethylene Carbonate Electrolyte Using Molecular Dynamics. *J. Phys. Chem. C* **2016**, *120*, 16322-16332.

(25) Núñez-Rojas, E.; González, I.; Guzmán-González, G.; Alejandre, J. Molecular dynamics simulations for liquid electrolytes of propylene carbonate with LiTFSI, LiPF6, and LiBF4 salts. *J. Mol. Liq.* **2023**, *390*, 122983.

(26) Saitoh, K.; Takai, Y.; Sato, T.; Takuma, M.; Takahashi, Y. Optimization of LIB Electrolyte and Exploration of Novel Compounds via the Molecular Dynamics Method. *Batteries-Basel* **2022**, *8*, 27.

(27) Ong, M. T.; Bhatia, H.; Gyulassy, A. G.; Draeger, E. W.; Pascucci, V.; Bremer, P.-T.; Lordi, V.; Pask, J. E. Complex Ion Dynamics in Carbonate Lithium-Ion Battery Electrolytes. *J. Phys. Chem. C* **2017**, *121*, 6589-6595.

(28) Borodin, O.; Smith, G. D. LiTFSI structure and transport in ethylene carbonate from molecular dynamics simulations. *J. Phys. Chem. B* **2006**, *110*, 4971-4977.

(29) Self, J.; Fong, K. D.; Persson, K. A. Transport in Superconcentrated LiPF6 and LiBF4/Propylene Carbonate Electrolytes. *ACS Energy Lett.* **2019**, *4*, 2843-2849.

(30) Kwon, Y.; Park, S. Complexation dynamics of CH3SCN and Li(+) in acetonitrile studied by two-dimensional infrared spectroscopy. *Phys. Chem. Chem. Phys.* **2015**, *17*, 24193-24200.

(31) Seki, S.; Hayamizu, K.; Tsuzuki, S.; Takahashi, K.; Ishino, Y.; Kato, M.; Nozaki, E.; Watanabe, H.; Umebayashi, Y. Density, Viscosity, Ionic Conductivity, and Self-Diffusion Coefficient of Organic Liquid Electrolytes: Part I. Propylene Carbonate + Li, Na, Mg and Ca Cation Salts. *J. Electrochem. Soc.* **2018**, *165*, A542-A546.

(32) Yuan, K.; Bian, H.; Shen, Y.; Jiang, B.; Li, J.; Zhang, Y.; Chen, H.; Zheng, J. Coordination Number of Li+ in Nonaqueous Electrolyte Solutions Determined by Molecular Rotational Measurements. *J. Phys. Chem. B* **2014**, *118*, 3689-3695.

(33) Yuan, R.; Yan, C.; Fayer, M. Ion-Molecule Complex Dissociation and Formation Dynamics in LiCl Aqueous Solutions from 2D IR Spectroscopy. *J. Phys. Chem. B* **2018**, *122*, 10582-10592.

(34) Kwak, K.; Zheng, J.; Cang, H.; Fayer, M. D. Ultrafast two-dimensional infrared vibrational echo chemical exchange experiments and theory. *J. Phys. Chem. B* **2006**, *110*, 19998-20013.

(35) Perdew, J. P.; Burke, K.; Ernzerhof, M. Generalized Gradient Approximation Made Simple. *Phys. Rev. Lett.* **1996**, *77*, 3865-3868.

(36) Kwak, K.; Rosenfeld, D. E.; Fayer, M. D. Taking apart the two-dimensional infrared vibrational echo spectra: more information and elimination of distortions. *J. Chem. Phys.* **2008**, *128*, 204505.

(37) Hoffman, D. J.; Fayer, M. D. CLS Next Gen: Accurate Frequency-Frequency Correlation Functions from Center Line Slope Analysis of 2D Correlation Spectra Using Artificial Neural Networks. *J. Phys. Chem. A* **2020**, *124*, 5979-5992.

(38) Deshmukh, S. H.; Nachaki, E. O.; Kuroda, D. G. Uncovering the binding nature of thiocyanate in contact ion pairs with lithium ions. *J. Chem. Phys.* **2024**, *161*, 034507.

(39) Yuan, R.; Fayer, M. D. Dynamics of Water Molecules and Ions in Concentrated Lithium Chloride Solutions Probed with Ultrafast 2D IR Spectroscopy. *J. Phys. Chem. B* **2019**, *123*, 7628-7639.

(40) Felsted, R. G.; Graham, T. R.; Zhao, Y.; Bazak, J. D.; Nienhuis, E. T.; Pauzauskie, P. J.; Joly, A. G.; Pearce, C. I.; Wang, Z.; Rosso, K. M. Anionic Effects on Concentrated Aqueous Lithium Ion Dynamics. *J. Phys. Chem. Lett.* **2024**, *15*, 5076-5087.

(41) Kramer, P. L.; Nishida, J.; Fayer, M. D. Separation of experimental 2D IR frequency-frequency correlation functions into structural and reorientation-induced contributions. *J. Chem. Phys.* **2015**, *143*, 124505.

(42) Wang, Y. Q.; Xu, H.; Cao, B.; Ma, J.; Yu, Z. W. In Situ Species Analysis of a Lithium-Ion Battery Electrolyte Containing LiTFSI and Propylene Carbonate. *J. Phys. Chem. Lett.* **2024**, *15*, 5047-5055.

(43) Mynam, M.; Ravikumar, B.; Rai, B. Molecular dynamics study of propylene carbonate based concentrated electrolyte solutions for lithium ion batteries. *J. Mol. Liq.* **2019**, *278*, 97-104.

(44) Yuan, R.; Napoli, J. A.; Yan, C.; Marsalek, O.; Markland, T. E.; Fayer, M. D. Tracking Aqueous Proton Transfer by Two-Dimensional Infrared Spectroscopy and ab Initio Molecular Dynamics Simulations. *ACS Cent. Sci.* **2019**, *5*, 1269-1277.

(45) Tan, H. S.; Piletic, I. R.; Fayer, M. D. Orientational dynamics of water confined on a nanometer length scale in reverse micelles. *J. Chem. Phys.* **2005**, *122*, 174501.

(46) Lipari, G.; Szabo, A. Model-free approach to the interpretation of nuclear magnetic resonance relaxation in macromolecules. 1. Theory and range of validity. *J. Am. Chem. Soc.* **1982**, *104*, 4546-4559.

(47) Lipari, G.; Szabo, A. Effect of librational motion on fluorescence depolarization and nuclear magnetic resonance relaxation in macromolecules and membranes. *Biophys. J.* **1980**, *30*, 489-506.

(48) Moog, R. S.; Ediger, M. D.; Boxer, S. G.; Fayer, M. D. Viscosity dependence of the rotational reorientation of rhodamine B in mono- and polyalcohols. Picosecond transient grating experiments. *J. Phys. Chem.* **2002**, *86*, 4694-4700.

(49) Hu, C.-M.; Zwanzig, R. Rotational friction coefficients for spheroids with the slipping boundary condition. *J. Chem. Phys.* **1974**, *60*, 4354-4357.

(50) Perrin, F. Mouvement brownien d'un ellipsoide - I. Dispersion diélectrique pour des molécules ellipsoidales. *J. Phys. Radium* **1934**, *5*, 497-511.

(51) Świergiel, J.; Płowaś, I.; Jadżyn, J. Charge Relaxation and Stokes–Einstein Relation in Diluted Electrolyte Solution of Propylene Carbonate and Lithium Perchlorate. *Ind. Eng. Chem. Res.* **2015**, *54*, 2108-2113.

(52) Hung, S. T.; Roget, S. A.; Zheng, W.; Fayer, M. D. Concentration Dependence of Dynamics and Structure among Hydrated Magnesium Ions: An Ultrafast Infrared Study. *J. Phys. Chem. B* **2023**, *127*, 3278-3290.

(53) Connolly, M. L. Solvent-accessible surfaces of proteins and nucleic acids. *Science* **1983**, *221*, 709-713.

(54) Yu, Z.; Wang, H.; Kong, X.; Huang, W.; Tsao, Y.; Mackanic, D. G.; Wang, K.; Wang, X.; Huang, W.; Choudhury, S.; et al. Molecular design for electrolyte solvents enabling energy-dense and long-cycling lithium metal batteries. *Nat. Energy* **2020**, *5*, 526-533.

(55) Zhu, M.; Wu, J.; Wang, Y.; Song, M.; Long, L.; Siyal, S. H.; Yang, X.; Sui, G. Recent advances in gel polymer electrolyte for high-performance lithium batteries. *J. Energy Chem.* **2019**, *37*, 126-142.

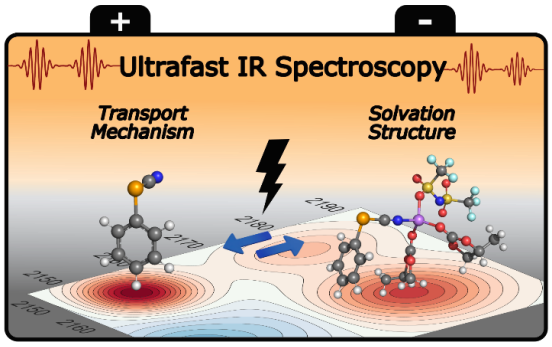

TOC Graphics